

Characterization of the High-Pressure and High-Temperature Phase Diagram and Equation of State of Chromium

Simone Anzellini (✉ simone.anzellini@diamond.ac.uk)

Diamond Light Source Ltd

Daniel Errandonea

Universidad de Valencia

Leonid Burakovsky

Los Alamos National Laboratory

John E. Proctor

University of Salford

Christine M. Beavers

Diamond Light Source Ltd

Research Article

Keywords: Characterization, high-pressure, high-temperature, phase diagram, equation, state of chromium, Birch-Murnaghan equations, thermal equation

Posted Date: December 30th, 2021

DOI: <https://doi.org/10.21203/rs.3.rs-1195199/v1>

License:  This work is licensed under a Creative Commons Attribution 4.0 International License.

[Read Full License](#)

Version of Record: A version of this preprint was published at Scientific Reports on April 25th, 2022. See the published version at <https://doi.org/10.1038/s41598-022-10523-2>.

Characterization of the high-pressure and high-temperature phase diagram and equation of state of chromium

Simone Anzellini^{1,*}, Daniel Errandonea², Leonid Burakovsky³, John E. Proctor⁴, and Christine M. Beavers¹

¹Diamond Light Source Ltd., Harwell Science & Innovation Campus, Diamond House, Didcot, OX11 0DE, UK

²Departamento de Física Aplicada - Instituto de Ciencia de Materiales, Matter at High Pressure (MALTA) Consolider Team, Universidad de Valencia, Edificio de Investigación, C/Dr. Moliner 50, Burjassot, 46100 Valencia, Spain

³Theoretical Divisions, Los Alamos National Laboratory, Los Alamos, New Mexico, 87545, USA.

⁴Materials & Physics Research Group, School of Science, Engineering & Environment, University of Salford, Manchester M5 4WT, United Kingdom

*simone.anzellini@diamond.ac.uk

ABSTRACT

The high-pressure and high-temperature melting curve of chromium has been investigated both experimentally (*in situ*), using a laser-heated diamond-anvil cell technique coupled with synchrotron powder X-ray diffraction, and theoretically, using *ab initio* density-functional theory simulations. In the pressure–temperature range covered experimentally (up to 90 GPa and 4500 K, respectively) only the solid body-centred-cubic and liquid phases of chromium have been observed. Experiments and computer calculations give melting curves in agreement with each other, that can be described by a Simon–Glatzel equation $T_m(P) = 2136K(1 + P/25.9)^{0.41}$. In addition, a quasi-hydrostatic equation of state at ambient temperature has been experimentally characterized up to 131 GPa and compared with the present simulations. Both methods give very similar third-order Birch–Murnaghan equations of state with a bulk modulus of 182–185 GPa and its pressure derivative of 4.74–5.15. According to the present calculations, the obtained melting curve and equation of state are valid at least up to 815 GPa, being the melting temperature at this pressure 9310 K. Finally, from the obtained results, it was possible to determine a thermal equation of state of chromium valid up to 65 GPa and 2100 K.

Introduction

Transition metals are the elements in the *d*-block of the periodic table, presenting a partially filled *d*-electron shell. They are characterized by having high: densities; cohesive energies; bulk moduli and melting temperatures. Many of them are refractory metals. Due to their typically high melting temperatures (T_m) and hardness, the technological applications and economic importance of these elements (and their alloys) is immense. From an engineering point of view, the need of controlling the properties of transition metal alloys has stimulated theoretical and experimental studies on the phase relations of the pure elements. These metals have also been the focus of fundamental research, mainly for understanding the influence of *d* electrons on the properties of the elements. On the other hand, the study of transition metals under high-pressure (*HP*) and high-temperature (*HT*) is extremely relevant for geophysics and planetary sciences as they represent the main constituents of planetary cores (*e.g.* Fe and Ni for Earth).¹ In particular, in the past two decades the characterization of the melting curves of transition metals has attracted the interest of many researchers around the globe. This is mainly due to the discrepancies observed in the melting temperatures obtained with different experimental (static and dynamic) and computational techniques. In particular, much effort has been devoted to try to solve the discrepancies observed in the extreme cases of Fe^{2–10}, Ta^{11–13}, Mo^{14–16} and Pt^{17–19}. The melting curve of other transition metals, like Nb, Ir, and V have been recently studied too^{20–22}.

In contrast with other transition metals, chromium (Cr) is one of the less studied elements of this group under *HP* – *HT* conditions. With an electronic configuration $3d^54s^1$, Cr belongs to the family of the *3d* transition metals (same as Mn, Fe, Co and Ni). It is a hard and brittle element, highly valued for its high resistance to corrosion. For this reason, it is used as the main additive in stainless steel and in other metallurgic processes. Under ambient conditions, Cr presents a body-centred-cubic (*bcc*) structure. At low *T* and *HP* the *bcc* structure of Cr is slightly modified by two first-order magnetic phase transitions.²³ From 0 K to 123 K, Cr is antiferromagnetic (AF) with a small tetragonal distortion of the *bcc* structure. Whereas, from 123 K to 311 K, it is AF with a small orthorhombic distortion of the *bcc* structure. These phase transitions have been measured to 0.8 GPa, but the lattice distortion of these phases is too small to be detected by X-ray diffraction (XRD).^{24,25} The physical

reasons for the ground state of Cr being AF have been discussed in several papers, *e.g.* in Asano and Yamashita,²⁶ arguments are provided to discuss the reasons for *bcc*-Fe being ferromagnetic (FM) but both *bcc*-Mn and *bcc*-Cr being AF. Above 311 K, Cr is paramagnetic (PM) and presents a *bcc* structure. According to theoretical calculations, Cr is expected to exhibit a *P*-induced polymorphism similar to both Mo and W, its partners in the periodic table, the *HP* crystal structure of which is double-hexagonal-close-packed (*dhcp*).²⁷ Indeed, a phase transition into hexagonal-close-packed (*hcp*) has been predicted for Cr, with transition *P* spanning from 7-12.5 Mbar.²⁸

The first static compression study of Cr at room-temperature (*RT*) was performed only up to 10 GPa^{29,30}. More recent studies on Cr-hydrates reported also synchrotron XRD measurements of pure Cr compressed to 40 GPa,^{31,32} providing information on its bulk modulus. None of these studies has shown any sign of occurrence of *P*-induced solid/solid phase transitions. Similar conclusions have been obtained from shock-compression studies up to 140 GPa³³. At ambient pressure Cr melts at 2136 K.³⁴ Differently from most of the other transition metals, the behaviour of Cr at *HP*-*HT* is still mostly unknown. The only reported melting curve of Cr was obtained two decades ago by Errandonea *et al.*³⁵ (along with the one of V and other transition metals) up to 60 GPa and 2600 K. It was determined from an experiment performed in a single-sided laser-heated (LH) diamond-anvil cell (DAC), using the speckle technique to detect melting. In this technique, a direct observation of movements on the sample surface, assigned to the transformation of solid Cr into liquid Cr, was used as melting diagnostic without any other structural characterization. Similarly to other cases obtained with the same method^{2,12,36}, the reported melting curve appeared to belong to the so called "low" melting curves^{37,38} which virtually flattens out at $P \sim 1$ Mbar and for which the T_m on the shock Hugoniot is much lower than that extracted from the shock compression data. Furthermore, the reported melting curve appeared to virtually coincide with the melting curve of V. The latter being recently very thoroughly re-measured using a state-of-the-art technique²² has been shown to be originally underestimated, now showing values belonging to the so-called "high" melting curves,^{37,38} in agreement with shock measurements. To the best of our knowledge, there are no computational studies of the melting curve of Cr reported yet.

From the results summarized above, it becomes clear how a proper characterization of the phase diagram of Cr at *HP*-*HT* is still lacking. For this purpose, we report a combination of *in situ* synchrotron XRD studies on Cr up to 131 GPa and 4500 K and density-functional theory (DFT) calculations aiming to characterize the phase diagram, melting curve, and thermal equation of state (EoS) of Cr.

Results and Discussion

Phase diagram

Eight *HP*-*HT* ramps were performed using the LH-system of the I15 beamline³⁹ at Diamond Light Source, investigating a *P*-*T*-range between 10-90 GPa and 300-4500 K, respectively. The *in situ* XRD analysis, revealed only the presence of the KBr-B2 phase (which acted as pressure medium and thermal insulator between sample and diamonds), and the *bcc* and the liquid phases of Cr in the investigated *P*-*T* range. Furthermore, the obtained data did not show any distortion of the *bcc* structure of Cr or evidence of the occurrence of any chemical reactions leading to the formation of oxides or carbides *e.g.* Cr₃C₂⁴⁰ or Cr₂O₃.⁴¹

During each experimental ramp, it was possible to study the textural evolution of the sample (and the insulating material) as a function of *P*-*T*. Figure 1 (a, b and c) shows an example of the textural evolution observed at around 45 GPa from ambient *T* up to 3853 K. In particular, the ambient *T* texture of KBr (highlighted in orange in the figure) does not change at 2935 K but it definitely shows some important thermal effect at 3853 K, evidenced by the reduction of the full width at half maximum (FWHM) of the 110 reflection of KBr-B2 and a general spottier appearance. The signal from Cr (highlighted in blue in the figure) shows a texture of an highly-oriented powder at 300 K. A temperature-induced re-crystallization, characterized by the presence of a spottier texture, can be observed at 2935 K. Furthermore at 3853 K, it is possible to observe how the single-crystal-like peaks from Cr are more angle-dispersed than the previous ones. This is caused by the presence of molten Cr in the signal and the geometry of the actual experimental setup. In fact, the scattered peaks of Cr are the one obtained from colder parts of the sample as explained in Anzellini *et al.*⁴² A better visualization of this behaviour can be obtained from the corresponding integrated signal of the pattern reported in Fig. 1d together with the patterns obtained at *T* just below and above 3853 K. In particular, it is possible to observe how at this *T* the XRD shows a diffuse signal caused by the appearance of liquid Cr. A further *T* increase, causes the appearance of an additional (and more intense) diffuse signal whose centre is shifted towards lower angles. We believe that this additional diffuse signal is caused by the melting of KBr. This observation is in agreement with the melting curve obtained in Briggs *et al.*⁴³ and plotted in Fig. 2 as continuous red line. Figure 2 reports the phase diagram of Cr as obtained in the present experiment, compared with previous experimental data. A diffuse signal in the integrated XRD pattern was observed in all the ramps performed between 10 GPa and 50 GPa and was considered as the appearance of liquid Cr (reported in the figure as light blue empty circle). However, we believe that the diffuse signal observed at 10 GPa is actually affected by the melting of KBr (as evidenced by the proximity of the reported KBr melting curve) and that

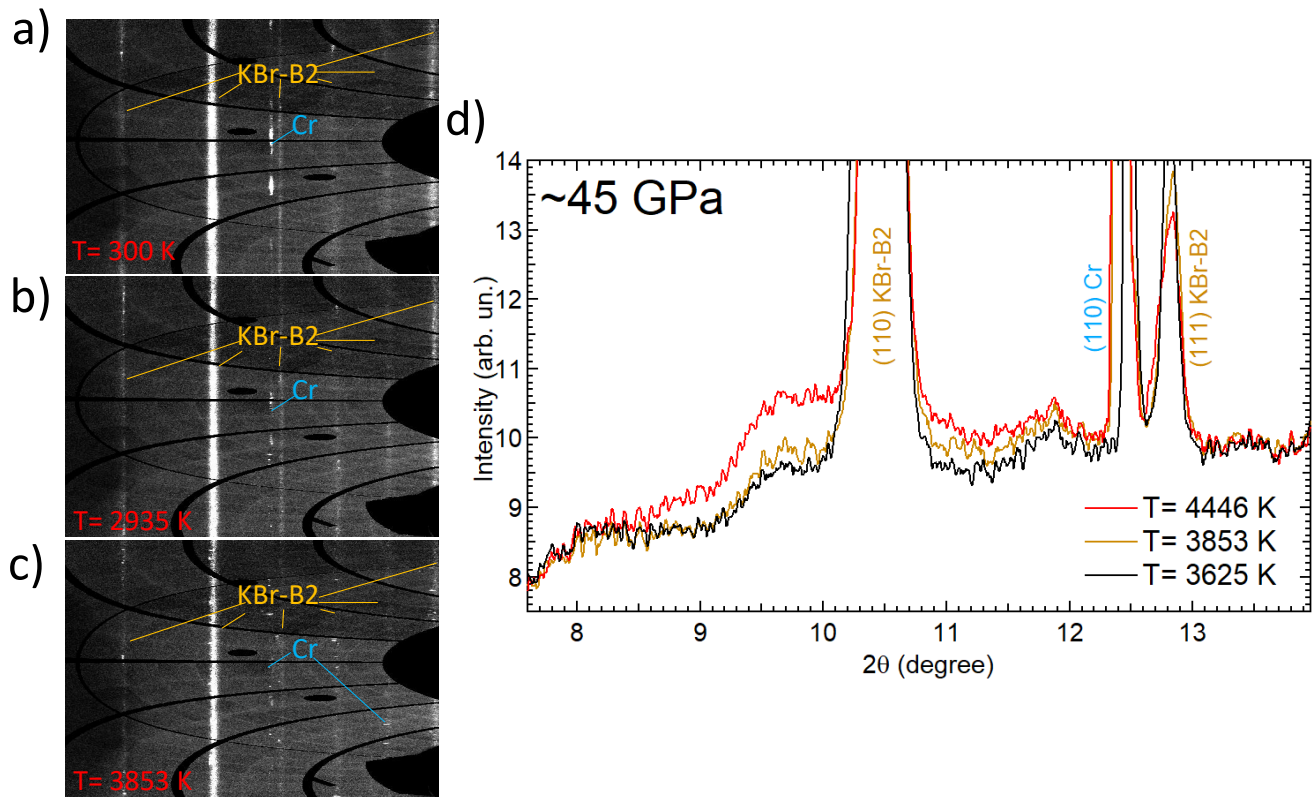


Figure 1. a,b,c) Unwrapped raw XRD images showing the textural evolution of a Cr sample embedded in KBr pressure transmitting medium at around 45 GPa. The signals arising from the different components are highlighted with different colours: blue for the Cr and orange for the KBr-B2. T is also indicated in red. d) Integrated XRD patterns at different T around 45 GPa. The onset of melting, characterized by the first appearance of diffuse signal, is observed at 3853 K (orange pattern). The diffuse scattering increases with the rising T , showing its maximum at 4446 K (red pattern)

is the reason why the reported T_m is lower than predicted by calculations and comparable to the melting temperature of Cr at ambient pressure.

During the ramps performed around 60 GPa and 70 GPa and T higher than 3200 K, we have noticed a misalignment in the optics of the heating system, causing T and XRD to be collected from different regions of the sample. This was also evidenced by the absence of thermal expansion in the lattice parameter of Cr. For these reason, all the data collected at T higher than 3200 K in these two ramps have been discarded as unreliable. Finally, we did not observed any diffuse signal in the ramp performed around 90 GPa, however, a plateau appeared in the T vs laser power plot at around 4000 K (reported as empty light green square in Fig.2) and we have decided to underline it as possible melting point as evidenced in previous LH-DAC experiments.^{17,21,36,44,45} The corresponding T_m is in agreement with our computer simulations. Additional off-line experiments were performed on Cr using the appearance of the plateau as melting criterion. For this purpose, the samples were prepared similarly to the one used for the experiments performed at the Diamond Light Source, but using MgO as insulating material (so to exclude any melting caused by the KBr). As for the experiments performed on I15, T was measured via spectral-radiometry, whereas P was measured from ruby fluorescence method at 300 K. The thermal P was estimated from the one observed on a previous XRD experiment performed using MgO as insulating material.²⁰ The melting temperatures obtained in these ramps are $(3500 \pm 150)\text{K}$ and $(4000 \pm 150)\text{K}$ at (55 ± 5) GPa and (90 ± 5) GPa, respectively and are reported in Fig.2 as empty pink squares.

The results obtained from the present simulation are reported in Fig.2 as solid green line and triangles and summarized in Table 1. In particular, six *bcc*-Cr melting points were calculated assuming a non-magnetic (NM) configuration, while other two were calculated assuming a paramagnetic (PM) *bcc*-Cr. From the obtained results it is clear that the melting curves of both PM-Cr and NM-Cr are virtually identical for the non-magnetic configuration points which are listed in Table 1. For each of the melting points, ten NVE (fixed total number of atoms N , system volume V , and total energy E ; V corresponds to one of the six densities from Table 1) runs of 10000-20000 time steps of 1.0 fs each were performed, with an increment of the initial T of

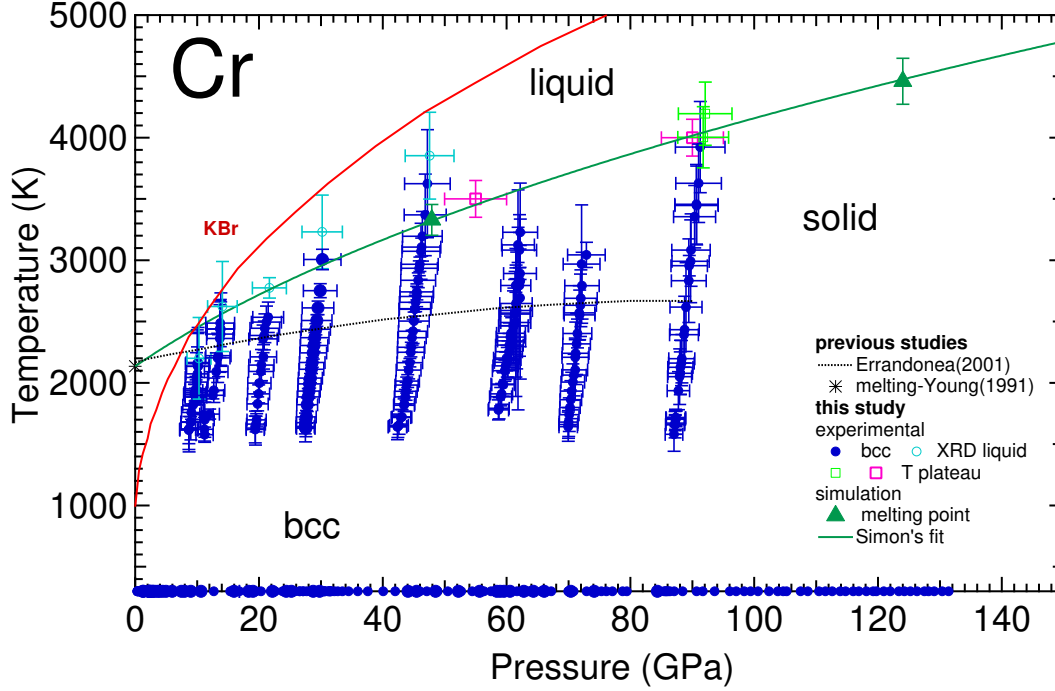


Figure 2. Phase diagram of Cr as obtained in the present study both experimentally (solid and empty circles and empty squares) and with first principle calculation (solid triangles and solid green line) and a previous study based on speckle³⁵ (dashed black line). The melting line of KBr as reported in Briggs *et al.*⁴³ is also represented as a continuous red line for reference.

Table 1. The six *ab initio* melting points of *bcc*-Cr, ($P_m, T_m \pm \Delta T_m$), obtained from the Z method implemented with VASP.

lattice constant (Å)	P_m (GPa)	T_m (K)	ΔT_m (K)
3.00	-5.2	1950	62.5
2.80	47.9	3330	125.0
2.65	124	4460	187.5
2.50	266	5840	187.5
2.35	526	7720	250.0
2.25	815	9310	250.0

125 K for the 1st, 250 K for the 2nd, 375 K for the 3rd and 4th, and 500 K for the 5th and 6th T_m . The corresponding error in T_m is half of the increment of the initial T ⁴⁶ so that it does not exceed $\sim 4\%$ in either case. The P errors are negligibly small: $\lesssim 0.5$ GPa for the first point, and 1-2 GPa for the remaining five. Hence, our melting results on *bcc*-Cr are very accurate.

Figure 3 and Fig. 4 offer an example of the present Z method melting simulations. They correspond to the third of the six T_m of Table 1, and show the time evolution of T and P , respectively, during the corresponding computer runs. During the $T_0 = 12125$ K run the system remains a super-heated solid: both the average T and P stay virtually the same during the 20 ps of running time. The $T_0 = 12500$ K run is the melting run during which a melting occurs: it starts after ~ 13 ps of running time, and the melting process takes about 3 ps. It results in the decrease of average T from ~ 5500 to 4460 K, and the corresponding increase of average P from ~ 118 to 124 GPa. This is so because the total energy, $E \sim k_B T + PV$, is conserved and V is fixed. For the same reason, Fig. 3 and Fig. 4 are “mirror images” of each other; see for more detail. In the run with higher $T_0 = 12875$ K, the melting starts after only 1 ps of running time. For a sufficiently high initial T the system melts virtually immediately.

From the analysis of Fig.2 it is possible to state that the present experimental and theoretical melting lines are in good agreement (within the experimental errors). The corresponding melting line can be described with a Simon-Glatzel equation¹ with the following expression $T_m(P) = 2136K(1 + P/25.9)^{0.41}$, where 2136 K is the T_m at ambient P as reported in Young.³⁴ This equation provides a good estimate of the melting line of Cr and describes properly both the experiments and the melting

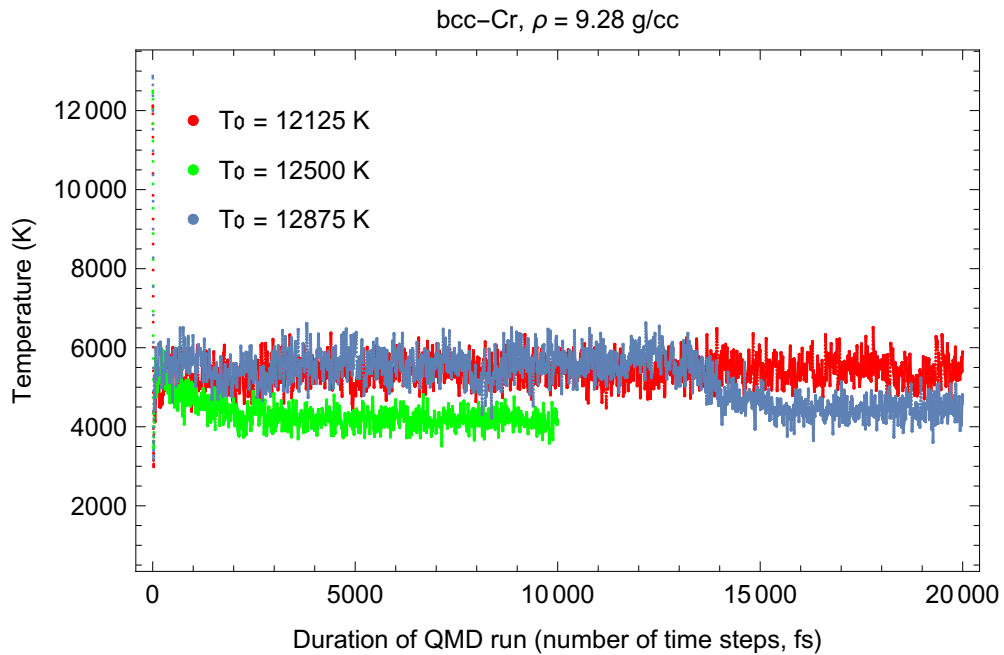


Figure 3. Time evolution of temperature in three QMD runs with initial temperatures (T_0) separated by 375 K. The middle run is the melting run during which T decreases from ~ 5500 K for the superheated state to 4460 K for the liquid at the corresponding melting point.

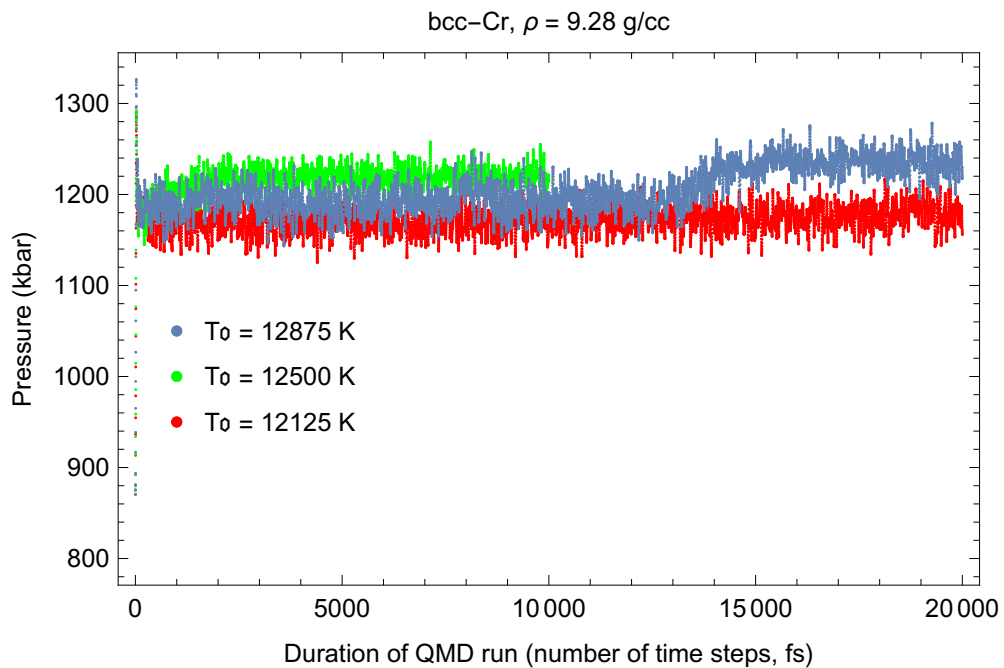


Figure 4. Time evolution of pressure in three QMD runs with initial temperatures (T_0) separated by 375 K. During melting P increases from ~ 120 GPa for the superheated state to 124 GPa for the liquid at the corresponding melting point.

temperatures calculated up to 815 GPa (9310 K). Notably the melting curve of Cr runs parallel to that of V²², the neighboring element in the periodic table. In particular, at low pressure the melting slope for Cr is dT_m/dP 34.9 K/GPa, while in V it is 32.6 K/GPa.

Let us now compare the melting slope to that given by the Clausius-Clapeyron (CC) formula $dT_m(P)/dP|_{P=0} = T_m(0) \cdot \Delta V_m / \Delta H_m$ with the experimental input. According to Stankus⁴⁷, the ambient melting density of liquid Cr is $\rho_L = 6.170 \text{ g/cm}^3$. This, along with the density of the solid before melting $\rho_S = 6.575 \text{ g/cm}^3$ leads to a volume change at melt $\Delta V_m = 0.519 \text{ cm}^3/\text{mol}$. According to another set of thermal expansion data on Cr⁴⁸, $\rho_L = 6.156 \text{ g/cm}^3$ and $\rho_S = 6.509 \text{ g/cm}^3$, so that $\Delta V_m = 0.458 \text{ cm}^3/\text{mol}$. Therefore, we are going to consider $\Delta V_m = 0.49 \pm 0.03 \text{ cm}^3/\text{mol}$. With the latent heat of melting of $\Delta H_m = 29 \pm 1 \text{ kJ/mol}$ (see above), the CC formula gives $dT_m(P)/dP|_{P=0} = 36.1 \pm 2.5$, which is in good agreement with both the present theoretical and experimental melting data. Another theoretical value of the initial slope, 33.5 K/GPa⁴⁹, is also consistent with the CC formula. We note that the use of $\Delta H_m = 21 \text{ kJ/mol}$ from⁵⁰ would result in the value of $dT_m(P)/dP|_{P=0}$ about 50% higher, which would contradict our experimental data. This strongly suggests that the assessment of ref.⁵⁰ is incorrect, including their value of $T_m(0) = 2180 \text{ K}$.

Finally, from the present *in situ* and computational characterization, it is possible to observe how the direct observation of movements on the sample surface as melting diagnostic³⁵ (dashed black line in Fig.2) is actually underestimating the melting curve of Cr. In particular, such an underestimation provides values going from being 8 % lower than the present one at 10 GPa to up to 34 % lower at 90 GPa. This confirms the unreliability of the speckle technique as melting diagnostic. In fact, there are elements for which the melting line obtained with this technique and by *in situ* XRD give similar values (e.g. Ca,⁵¹ Pt,¹⁷ Al⁵² and Cu⁵³). However, in most of the cases, the melting line obtained via speckle technique underestimates (some times by thousands of K) the melting line of the studied elements ((e.g. Fe², Ni³⁶, Ta¹², Mo¹⁵, etc..) and Cr is one of them.

Cold compression curve

A cold compression run was carried out at *RT* at the extreme conditions beamline (I15) of Diamond Light Source under quasi-hydrostatic conditions (using Helium (He) as pressure transmitting medium). The experiment was performed up to 131 GPa and the obtained unit-cell parameters at each pressure are reported in Table 2. In the entire investigated *P* range, Cr maintains its *bcc* structure. When analyzing the XRD patterns of Cr, special attention was taken to the possible occurrence of a *P*-induced rhombohedral distortion, as observed in V at 60 GPa.²² This distortion causes a splitting in the 211 reflection. In the present study we observed that such a splitting does not take place, indicating that the cubic-rhombohedral transformation does not take place in Cr up to at least 131 GPa.

Figure 5 shows the azimuthally-unwrapped raw images and the corresponding integrated patterns obtained at the lowest and the highest *P* reached in this experiment. From an analysis of the unwrapped images it is possible to observe how the texture of Cr evolves from a powder-like signal with some preferred orientations at ambient conditions, into a more spotty (highly oriented) signal at 131 GPa. The pattern in Fig. 5a was collected before He loading. In this way it was possible to check the quality of the loading before starting the actual experiment and to obtain a perfect V_0 to use for the EoS fitting. In both cases it is possible to observe the presence of Re signal (labelled with asterisks in Fig. 5a and Fig.5c) due to the small diameter of the gasket hole and the high divergence of the X-rays focusing on I15's micro-focus station. This causes an interaction between the tails of the X-rays beam and the Re edge of the micro-metric high-pressure chamber. At *HP* it is also possible to observe a splitting of the Re peaks into two groups, one at the same *P* as the sample (black asterisk in Fig. 5c), according to the Re EoS of Anzellini *et al.*⁵⁴ and one at lower *P* (red asterisk in Fig. 5c). Such a behaviour has been also observed in recent experiments performed with toroidal DACs⁵⁵. It is probably due to a combination of effects caused by the *P*-induced deformation of the gasket and the presence of the above-discussed X-ray tails. In fact, due to the corresponding shrinking of the high pressure chamber, the X-rays are now probing both the gasket in contact with He (same pressure as the sample) and the one directly squeezed between the anvils. In Fig.5c it is also possible to observe the presence of a peak around $2\Theta = 19$ degrees due to solid He. Such a peak appeared for the first time around 26 GPa and its behaviour under compression agreed perfectly with the He EoS of Loubeyre *et al.*⁵⁶ When possible, the 110, 200 and 211 reflections of *bcc* Cr were used in the Pawley refinement to obtain its lattice parameter. However, with increasing pressure, the 200 and 211 started overlapping with peaks from Re, leaving 110 as the only usable peak. Thanks to the cubic nature of Cr, this did not create a problem for the present characterization.

A qualitative analysis of the hydrostatic conditions of the sample was performed by comparing the *d*-spacing of Cr measured at the highest *P* reached in the present experiment with the theoretical one obtained using the same lattice parameter. The observed deviation of 0.01 % is well inside the beamline's resolution power obtained from a similar analysis of the signal from the CeO₂ standard at ambient *P*. That means that any possible deviation from hydrostaticity is too small to be experimentally detected. Therefore, we can consider the present compression curve as quasi-hydrostatic.

The present DFT calculations show that the (*P*=0, *T*=0) ground state corresponds to a *bcc*-Cr density of 7.229 g/cm³ (a lattice constant of 2.88 Å or an atomic volume of 23.888 Å³), or a molar volume of 7.193 cm³, in excellent agreement with 7.2 cm³ from the present and previous experiments⁵⁷. At this density, the NM *bcc*-Cr is higher in energy by $\sim 20 \text{ meV/atom}$,

i.e., the ground state of *bcc*-Cr is correctly predicted to be antiferromagnetic (AF). However, the calculated magnetic moment per atom (MMA), $\sim 1.1 \mu_B$ is somewhat larger than the experimental $0.62 \mu_B$ ⁵⁸ which is a typical discrepancy for this type of theoretical calculations^{58,59}. MMA depends almost linearly on the *bcc*-Cr lattice constant, a : $\mu(a) \approx 1.1 + 14(a - 2.88)$, and turns zero at $a \approx 2.8 \text{ \AA}$ (a density of 7.87 g/cm^3). The corresponding P is $\sim 22 \text{ GPa}$. This is higher than, respectively, $\approx 2.84 \text{ \AA}$ and $\approx 10 \text{ GPa}$ where the experimental Néel T , as $T = T(a)$ and $T = T(P)$, turns zero⁶⁰, but consistent with another theoretical work⁵⁹ which demonstrates that the calculated magnetic moment is suppressed considerably at a pressure of $\sim 20 \text{ GPa}$. At $P \gtrsim 20 \text{ GPa}$ the EOS of AF *bcc*-Cr merges into that of non-magnetic (NM) *bcc*-Cr, so that the two EoSs are virtually identical. Both AF *bcc*-Cr below 20 GPa and NM *bcc*-Cr above 20 GPa combined are described by the third-order Birch-Murnaghan EoS. The EoS parameters are summarized in Table 3. This EOS is expected to be reliable to $\sim 2 \text{ TPa}$.

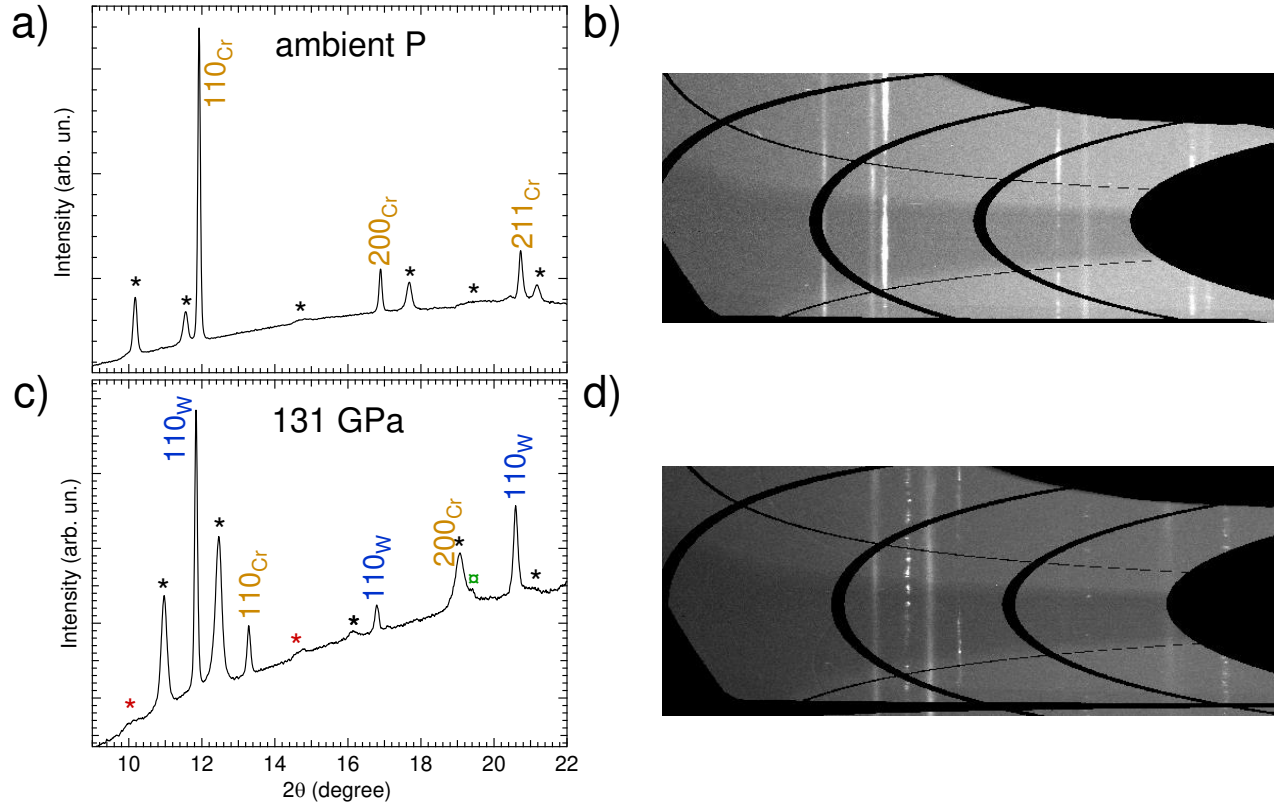


Figure 5. Integrated powder XRD patterns of Cr at the lowest (a) and the highest (b) P reached in the present experiment and their corresponding image plates (c) and (d), respectively. The different coloured asterisks are indicating the peaks from the Re gasket. The empty green symbol labels the peak obtained from solid He. The pattern in (a) was collected before the He loading and the DAC was positioned to get only the signal from Cr. In (c) the DAC was positioned differently so to get signals from both Cr and W simultaneously.

We note that in the above EOS paramagnetic (PM) Cr is not included explicitly. To check the possible influence of this in the present results, we did calculate the EoS of PM *bcc*-Cr using the GGA+U scheme with spin-orbit coupling suggested for the calculation of the properties of paramagnetic materials.⁶² We used the Dudarev approach⁶³ in which the parameters U and J do not enter separately since only their difference $U - J$ is meaningful. The value of $U - J = 4.5 \text{ eV}$ (actually, $U = 4.5 \text{ eV}$ and $J = 0$) comes from⁶⁴. We found that the EoS of PM *bcc*-Cr virtually coincides with that of NM *bcc*-Cr, because the difference in the two values of P at the same density becomes negligibly small as density increases. Since their EoSs are virtually identical, too, it does not really matter what structure of *bcc*-Cr is considered: paramagnetic or nonmagnetic.

Table 2. The unit-cell parameters of Cr at ambient T as a function of P . All values are obtained using He as pressure transmitting medium. The lattice parameter of W used for the P^{61} measurement are also reported. Experimental uncertainty on lattice parameters is lower than 0.003 Å. Uncertainty on pressure measurement increases from 0.06 GPa at ambient P to 0.27 GPa at 200 GPa.

a_W (Å)	P_W (GPa)	a_{Cr} (Å)	V_{Cr} (Å ³)	a_W (Å)	P_W (GPa)	a_{Cr} (Å)	V_{Cr} (Å ³)	a_W (Å)	P_W (GPa)	a_{Cr} (Å)	V_{Cr} (Å ³)
3.167	0.00	2.886	24.03	3.042	45.97	2.730	20.34	2.926	114.75	2.612	17.82
3.165	0.40	2.884	24.00	3.039	47.09	2.726	20.27	2.925	116.00	2.610	17.78
3.165	0.32	2.884	23.99	3.036	48.86	2.723	20.18	2.923	116.89	2.609	17.75
3.165	0.38	2.884	23.99	3.032	50.50	2.719	20.10	2.922	118.11	2.608	17.73
3.165	0.38	2.884	23.98	3.028	52.65	2.714	19.99	2.920	119.22	2.606	17.70
3.165	0.47	2.884	23.98	3.024	54.44	2.711	19.92	2.920	119.73	2.605	17.68
3.165	0.51	2.884	23.98	3.021	56.35	2.707	19.85	2.918	120.94	2.603	17.64
3.164	0.65	2.884	23.98	3.019	57.48	2.704	19.77	2.917	121.94	2.602	17.62
3.164	0.66	2.884	23.98	3.014	59.77	2.700	19.68	2.915	123.36	2.601	17.59
3.163	0.94	2.883	23.96	3.011	61.66	2.697	19.62	2.914	124.25	2.600	17.57
3.161	1.38	2.880	23.89	3.008	62.95	2.695	19.57	2.912	125.21	2.598	17.53
3.149	5.18	2.862	23.44	3.007	63.55	2.693	19.54	2.911	126.29	2.597	17.51
3.125	12.71	2.832	22.72	3.003	65.60	2.688	19.41	2.909	127.49	2.595	17.48
3.117	15.34	2.822	22.48	3.002	66.34	2.686	19.37	2.909	128.17	2.594	17.46
3.107	18.86	2.809	22.16	3.000	67.19	2.684	19.34	2.907	129.07	2.593	17.43
3.106	19.49	2.806	22.10	2.995	69.94	2.680	19.26	2.906	130.34	2.592	17.41
3.103	20.32	2.803	22.03	2.995	70.08	2.679	19.23	2.905	131.39	2.590	17.38
3.097	22.63	2.797	21.88	2.994	70.61	2.678	19.20				
3.094	23.80	2.794	21.81	2.990	72.92	2.675	19.14				
3.091	24.87	2.791	21.75	2.988	74.05	2.673	19.09				
3.090	25.51	2.789	21.70	2.986	75.29	2.671	19.05				
3.089	25.62	2.787	21.66	2.985	76.12	2.669	19.02				
3.089	25.82	2.786	21.62	2.983	77.09	2.668	18.98				
3.087	26.57	2.785	21.59	2.980	78.74	2.665	18.94				
3.087	26.60	2.783	21.56	2.979	79.40	2.664	18.91				
3.085	27.15	2.782	21.54	2.969	85.41	2.654	18.70				
3.085	27.10	2.781	21.51	2.969	85.67	2.654	18.69				
3.084	27.68	2.780	21.49	2.969	85.70	2.654	18.69				
3.083	28.24	2.779	21.46	2.969	85.92	2.653	18.68				
3.082	28.48	2.777	21.42	2.968	86.09	2.653	18.68				
3.082	28.46	2.777	21.42	2.968	86.40	2.653	18.67				
3.081	29.03	2.775	21.36	2.967	87.07	2.651	18.64				
3.077	30.64	2.772	21.30	2.965	88.41	2.649	18.59				
3.077	30.54	2.771	21.29	2.961	90.68	2.647	18.54				
3.077	30.48	2.771	21.28	2.960	91.68	2.645	18.51				
3.077	30.69	2.771	21.27	2.957	93.60	2.643	18.45				
3.075	31.22	2.770	21.26	2.953	96.04	2.640	18.40				
3.075	31.15	2.770	21.25	2.951	97.09	2.638	18.36				
3.075	31.43	2.769	21.24	2.949	98.36	2.636	18.31				
3.074	31.68	2.769	21.22	2.948	99.39	2.634	18.27				
3.074	31.54	2.768	21.21	2.946	100.6	2.632	18.23				
3.075	31.40	2.768	21.20	2.944	102.37	2.629	18.18				
3.073	32.17	2.767	21.17	2.942	103.79	2.627	18.14				
3.072	32.74	2.765	21.14	2.940	104.66	2.626	18.11				
3.070	33.48	2.763	21.09	2.940	105.22	2.625	18.09				
3.068	34.46	2.760	21.02	2.936	107.49	2.622	18.03				
3.064	35.95	2.755	20.91	2.935	108.64	2.620	17.99				
3.060	37.59	2.751	20.83	2.932	110.45	2.617	17.92				
3.055	40.06	2.745	20.69	2.931	111.50	2.616	17.91				
3.050	42.00	2.740	20.57	2.929	112.58	2.615	17.88				
3.045	44.40	2.734	20.45	2.927	113.87	2.613	17.84				

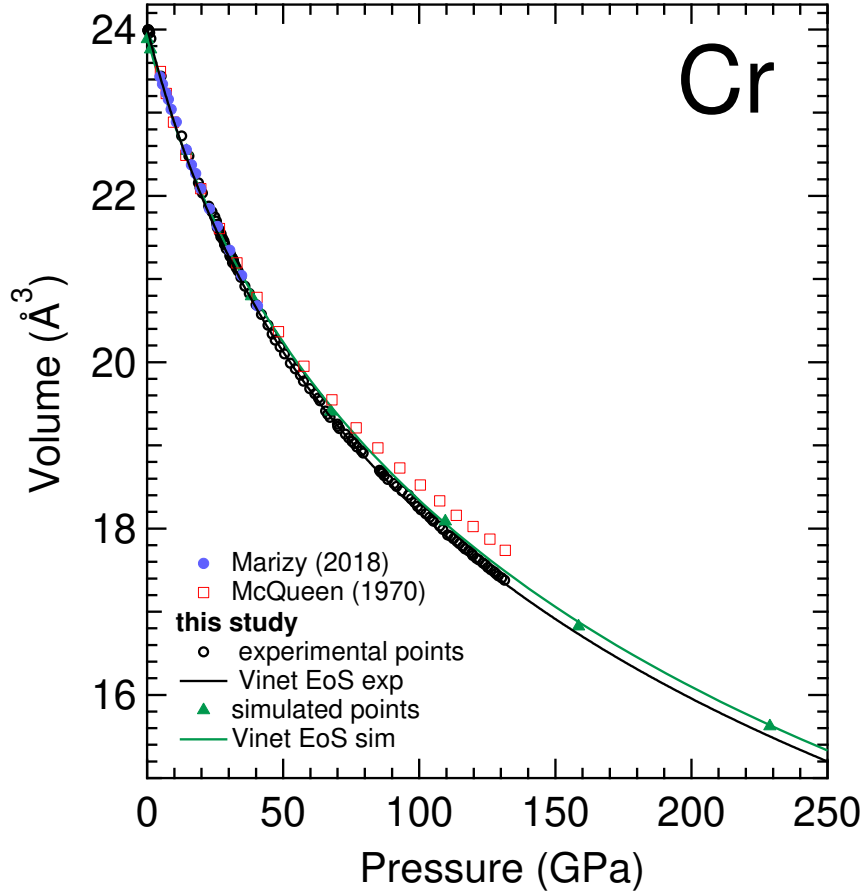


Figure 6. Measured and calculated volume of chromium as a function of P compared with the shock data of McQueen³³ and the XRD data of Marizy *et al.*³²

The obtained experimental ambient T compression curve is reported in Fig.6. The results are compared with the present theoretical calculations and previous experimental results obtained from static³² and dynamic³³ studies. From an analysis of the figure, it is possible to observe how the present results are in agreement with those previously obtained in a DAC experiment performed under the same conditions³². On the other hand, it is also clear how the data reduced from the shock experiment reported by McQueen *et al.* start diverging from the present data at around 33 GPa. Providing a volume that goes from being 0.5 % higher than the present one at 33 GPa to 2 % higher at 130 GPa. Such a difference, being small, it is probably caused by the rise of the sample temperature during shock compression.

The present compression curve has been fitted with a third order Vinet and Birch-Murnaghan EoS (BM3) using the EOSFit7 software⁶⁵. The corresponding bulk moduli K_0 , their pressure derivative K'_0 and volumes V_0 at ambient P are reported in Table 3 and compared with previous results. In the table it can be seen that calculations slightly underestimate the volume at ambient conditions, but are in excellent agreement with experiments regarding the bulk modulus and its pressure derivative. In particular, the values obtained from calculations are within the 68.3% confidence level ellipse of the experimental results. When the bulk modulus is compared with previous studies it can be seen that among previous DAC experiments the experiment of Marizy *et al.*³² reported a bulk modulus 10 % larger than the present one; but reported a smaller pressure derivative for the bulk modulus. However, their parameters fall within the 95.5% confidence level ellipse of the experimental results; i.e. we can conclude that there is a good agreement between both experiments. The small difference in the EoS parameters could be related to the use of a different pressure standard or to the different pressure ranges covered by both experiments. Shock-wave experiments also found a bulk modulus in good agreement with the present results. In contrast, the experiment by Ming *et al.*²⁹ gives an overestimated bulk modulus. In fact, their values for K_0 and K'_0 are outside the 99.7 % confidence level ellipse of our results. Their overestimation of the bulk modulus could be related to the highly non-hydrostatic conditions of their experiments which were carried out without any pressure transmitting medium. Finally, previous DFT calculations also overestimate the

Table 3. EOS parameters of Cr measured and calculated in different experiments. The volume V_0 , the bulk modulus K_0 and its pressure derivative K'_0 are listed. Experimental methods and EOS formulation are specified. PTM: Pressure transmitting medium. BM3: third order Birch-Murnaghan. ED-XRD: Energy dispersive X-ray diffraction. AD-XRD: Angular dispersive X-ray diffraction

Reference	V_0 (\AA^3)	K_0 (GPa), K'_0	PTM	Pressure gauge	EOS	Method
this study	24.08(2)	185(1), 4.74(3)	He	W ⁶¹	BM3	AD-XRD in DAC
this study	24.08(3)	182(1), 5.10(4)	He	W ⁶¹	Vinet	AD-XRD in DAC
³²	24.00(2)	200(2), 4.3(8)	He	not specified	Vinet	AD-XRD in DAC
²⁹		245(7), 5.5	none	not specified	BM3	ED-XRD in DAC
³³		175(3), 6.18(9)			Vinet	Shock
this study	23.9	182.4, 5.15			BM3	LDA NM
this study	23.9	182.2, 5.16			BM3	LDA PM
³²	23.1(1)	258.0(5), 4.30(1)			Vinet	DFT

bulk modulus. This can be related to an overestimation of the cohesive energy due to the functionals they used to describe the exchange–correlation of the energy. To conclude the discussion on the bulk modulus we will compare Cr with other *bcc* transition metals. We have noticed when comparing group 4 and 5 (3d and 4d) transition metals, that the corresponding bulk moduli increase following the sequence V (143) < Nb (170) < Cr (185) < Mo (210). As a consequence Cr is one of the hardest among them, being the sequence of their Vickers hardness also the same V (60 Hv) < Nb (75 Hv) < Cr (90 Hv) < Mo (120 Hv).⁶⁶

Thermal equation of state

In Fig. 7 the measured volumetric compression is reported as a function of P for different T . The ambient T data points correspond to results shown in Table 2. From the P – V – T data shown in Fig. 7, it was possible to determine a thermal EoS taking advantage of the EoSFit7 package⁶⁵. The established P – V – T EoS is valid up to 65 GPa. For the analysis, we have used all the data included in the figure. During the fitting procedure, the third-order BM EoS generated from the RT compression experiment has been used as the isothermal part of the P – V – T EoS. In addition, a Berman equation has been employed as the thermal-expansion model,⁶⁷ assuming a linear variation of K_0 with T . The pressure derivative of the bulk modulus has been assumed to be P -independent. On the other hand, the thermal expansion has been considered to be P -independent and to have a linear T -dependence. This simple model properly describes all the available experimental results, up to 2100 K, as it can be seen from the figure. The model does not reproduce very well the results at 2600 K and 2700 K, probably because of the influence on anharmonic effects at such T , which are not considered. The obtained parameters are $dK_0/dT = -0.022(9)$ GPa/K, volumetric thermal expansion $\alpha = 3.0(5)10^{-5}\text{K}^{-1}$, and $d\alpha/dT = 1.5(5) \times 10^{-9}\text{K}^{-2}$. They are comparable to the values of the same parameters reported for *bcc* vanadium²², *fcc* platinum¹⁷ and iridium²⁰, and *hcp* ruthenium⁶⁸. This makes us confident in the P – V – T EoS parameters determined in the present work for chromium. These parameters can be used for calculating higher-order thermoelastic parameters; for instance αxK and $(dK/dT)_V = (dK/dT)_P + \alpha xK(dK/dP)_T$. From the present results, we obtained that $\alpha xK = 0.0055$ K/GPa and $(dK/dT)_V = 0.0043$ GPa/K. This small value of αxK_0 indicates that the thermal pressure in Cr is small, therefore Cr can be used as calibrant in HP – HT experiments. On the other hand, $(dK/dT)_V$ is close to zero, which is in agreement with the Swenson law.⁶⁹ The positive value obtained implies that the thermal pressure slightly increases with compression.

Conclusions

In the present study, we have determined the P – T phase diagram of chromium up to 90 GPa and 4500 K, respectively, combining LH-DAC and synchrotron-based XRD. We have also explored it by DFT calculations up to 275 GPa and 5830 K. Experiments and calculations are in complete agreement and the obtained melting temperature as a function of P can be described with a Simon–Glatzel equation $T_m(P) = 2136K(1 + P/25.9)^{0.41}$. We have also found that Cr remains in the *bcc* phase up to 131 GPa and determined a P – V equation of state from which a bulk modulus of 182–185 GPa has been established. We have also determined the volume of Cr as a function of P following different isotherms, obtaining a P – V – T equation of state, allowing Cr to be used as a pressure standard for HP – HT experiments. Finally, DFT calculations supports that the determined melting curve is valid up to extreme pressures close to 1 TPa.

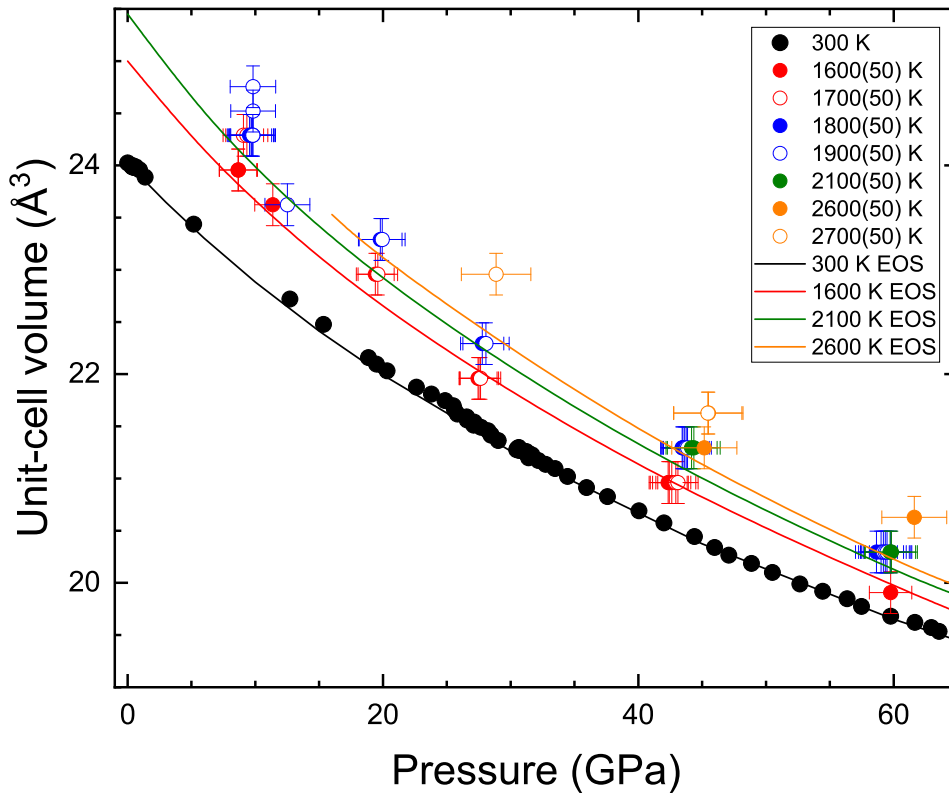


Figure 7. Unit-cell volume of Cr versus pressure for different temperatures. Different symbols correspond to different temperatures which are indicated in the figure. The solid lines are isotherms obtained from the P–V–T EoS we determined. The 2600 K isotherm of Bcc Cr is shown only for $P > 16$ GPa because at lower pressure Cr is liquid.

Methods

Experimental

Four membrane diamond anvil cells (DAC) were equipped with diamond with culets ranging from $100 \times 300 \mu\text{m}$ to $400 \mu\text{m}$. The gaskets were prepared from pre-indented and sparkle-eroded Re foils ($200 \mu\text{m}$ original thickness). For both the high and the ambient T experiments the sample were taken from a $\geq 99\%$ trace metal basis from Sigma Aldrich. For the laser-heating experiments, the Cr powder was squeezed between two diamond anvils to obtain a foil of $\sim 2 \mu\text{m}$ thickness. The foil was then cut to the desired size and loaded in the DAC high pressure chamber between two disks of KBr. The KBr disks, oven dried at 250°C for a couple of hours before the actual loading, were used as: pressure transmitting medium; to insulate the sample from the diamond anvils (thermally and chemically) and as pressure gauge.

In order to maximize the hydrostatic conditions, few grains of Cr were loaded at the centre of the DAC's high pressure chamber used for the cold compression experiment. A grain of W was also added few μm from the Cr sample as X-ray standard. W was chosen due to its high X-ray scattering power and well characterized EoS, attested by the consistency between static, dynamic and ultrasonic measurements.^{70,71} Finally, once the quality of the loading was attested by XRD (also used to obtain the actual V_0 of Cr), the high pressure chamber was filled with He pressure transmitting medium.

Both experiments were performed at the extreme conditions beamline I15 of Diamond Light Source.⁷² The beamline's polychromatic beam was tuned to 29.20 keV and 29.25 keV for the laser-heating and cold compression experiments, respectively. In both cases the beam was focused down to $9 \times 6 \mu\text{m}^2$ (FWHM) and a Pilatus CdTe 2M detector was used to ensure fast data collections with a good signal/noise ratio. In both cases, the sample-to-detector distance was calibrated following standard procedure from the diffraction ring of a CeO_2 standard.

Laser-heating

The HP-HT experiments were performed using the beamline's laser-heating system⁷², following the procedure described in Anzellini *et al.*¹⁷ Before each heating ramp, the sample was brought to the target P , measured from the compression curve of KBr, according to the thermal EoS of Dewaele *et al.*⁷³ In order to minimize axial thermal gradients on the sample, double sided laser-heating were performed using two 100 W Nd:YAG lasers. Both lasers were individually focused on the sample's surfaces and tuned in order to obtain similar T values. Both lasers were slightly unfocused (towards the sample) and coupled together, in order to increase the FWHM of their Gaussian profile on the sample surfaces and maximise the region at uniform T ($\sim 40\mu\text{m}$) probed by the X-rays. During the experiment, T was measured via spectral radiometry (between 450-950 nm), following the procedure described in Anzellini *et al.*⁴² T were simultaneously collected from both sides of the sample and the final T was considered as the average between the two. The resulting error in each T measurement was assumed to be the maximum values between the difference of T measured from the two sides of the sample and the standard deviation of the histograms obtained from their two-colours pyrometries (Benedetti and Loubeyre⁷⁴). The corresponding thermal P was obtained from the thermal EoS of Dewaele *et al.*⁷³ under the assumption that Cr and KBr were experiencing the same T . Considering the present sample geometry and the corresponding axial thermal gradient, the maximum error in P was calculated as half the difference between the pressure obtained from the KBr at the measured T (when in contact with the Cr) and the one from the KBr at ambient T (when in contact with the diamond). Before and after each heating ramp, the alignment between the X-rays, the lasers and the T reading was checked following the procedure described in Anzellini *et al.*⁷²

The heating ramps were performed in "trigger mode": both lasers were set to a target power; after 0.3 s a diffraction pattern and a T measurement were collected simultaneously; 0.3 s after the XRD collection, both laser powers were set back to zero. This procedure allowed us to minimize the interaction time between the laser and the sample (reducing the risk of possible chemical reactions) and to perform any adjustment in the optics when needed.⁴²

During each heating ramp, the lasers powers were increased until a diffuse signal (characteristic of liquids) was detected in the diffraction pattern or it was not possible to further increase T , probably due to change in the insulating conditions of the sample *e.g.* presence of a laser-drilled hole.

Several heating ramps were performed on the same samples at different P - T conditions. In order to avoid any chemical contamination, each ramp was performed on a different region of the sample and the quality of the selected region was first checked via XRD before the actual ramp.

During the analysis procedure, good care was taken to investigate the different aspects of the experiment. T measurements were double checked following the procedure described in Benedetti and Loubeyre⁷⁴. An accurate analysis of the diffraction patterns was performed to detect the appearance of the melting and to obtain structural and textural information about the sample and the insulating material. Masks were applied on a per-image basis and the images azimuthally integrated using the DIOPTAS suite⁷⁵. KBr data were treated as powder data and a Pawley analysis was performed with the TOPAS suite⁷⁶ using previously reported parameters as starting values. A similar analysis was originally performed for Cr. However, in order to account for the experimental thermal gradients, the thermal expansion data of Cr were obtained treating the XRD as single crystal data. A single peak of Cr (corresponding to the 110 plane) was followed during heating and integrated individually to determine the corresponding lattice parameter.

Finally, the structural measurement were compared to the T ones so to obtain a detailed *in situ* and "time-resolved" analysis of the sample evolution as a function of P and T .

Cold compression

During the cold compression experiment, P inside the high pressure chamber was estimated from the measured volume of the W X-ray standard following the calibration of Dorogokupets *et al.*⁶¹ According to the adopted pressure scale, the error in the present P measurements goes from 0.06 GPa at ambient P and reaches 0.27 GPa at 200 GPa. During the entire compression run we tried to maintain pressure steps of the order of 0.5 - 1 GPa, with a stabilization period of 2 min between each XRD measurement. Diffraction data were azimuthally integrated using the DIOPTAS suite⁷⁵, with mask applied on a per-image basis. The obtained diffraction patterns were analysed by Pawley fitting using the routines of the TOPAS software suite⁷⁶, literature values for the lattice parameters were used as starting points for the refinement.

Theoretical calculations

Our theoretical calculations of the equation of state and melting curve of Cr are based on density-functional theory (DFT) with the projector-augmented-wave (PAW)⁷⁷ implementation and the generalized gradient approximation (GGA) for exchange-correlation energy, in the form known as Perdew-Burke-Ernzerhof (PBE)⁷⁸. For these calculations Vienna *Ab initio* Simulation Package (VASP) was used. The reason for choosing GGA instead of another implementation of DFT, namely, local density approximation (LDA) is that it has been known that LDA does not accurately describe the properties of 3d transition metals, specifically, chromium for which its predictions are in drastic disagreement with experiment^{79,80}, and iron for which it produces a wrong ground state: AF or nonmagnetic (NM) *bcc*^{81,82} or NM-*hcp*⁸³⁻⁸⁵ instead of FM-*bcc*. LDA also fails in assessing the

strength of the magnetovolume effect. On the other hand, GGA correctly predicts the structural and magnetic phase diagrams⁸⁶. Since the simulations were performed at *HP–HT* conditions, we used accurate pseudopotential where the semi-core 4s and 4p states were treated as valence states. Specifically, Cr was modeled with 12 valence electrons per atom (3p, 3d, and 4s orbitals). The core radius (the largest values of RCUTs among those or each of the quantum orbitals) for this pseudopotential is 2.3 a.u., or 1.22 Å. Numerical errors in the calculations using VASP will remain almost negligible until the nearest neighbor distance reaches $2 \times \text{RCUT} / (1.25 \pm 0.05)$ ⁸⁷. Hence, with these pseudopotential, one can study systems with densities up to $\sim 22 \text{ g/cm}^3$, at least at low T . With our EoS of Cr, this corresponds to P above 2 TPa. A cold ($T = 0$) EOS was calculated using unit cells with a very dense k -point mesh of $50 \times 50 \times 50$ for high accuracy. The AF bcc-Cr was studied in the framework of fully unconstrained noncollinear magnetism developed in ref.⁸⁶. The theoretical melting curve of chromium was calculated via *ab initio* quantum molecular dynamics (QMD) simulations using the Z method implemented with VASP which is described in detail in Refs.^{19,46,88} We used a 432-atoms ($6 \times 6 \times 6$) bcc-Cr supercell with a single Γ -point. Full energy convergence (to $\lesssim 1 \text{ meV/atom}$) was checked for each simulation. For the calculation of the melting curve the nonmagnetic structure is considered.

Data Availability

The datasets generated during and/or analysed during the current study are available from the corresponding author on reasonable request.

References

1. Poirier, J.-P. *Introduction to the Physics of the Earth's Interior* (Cambridge University Press, 2003).
2. Anzellini, S., Dewaele, A., Mezouar, M., Loubeyre, P. & Morard, G. Melting of iron at Earth's inner core boundary based on fast X-ray diffraction. *Science* **340**, 464–6 (2013).
3. Boehler, R., Santamaría-Pérez, D., Errandonea, D. & Mezouar, M. Melting, density, and anisotropy of iron at core conditions: new X-ray measurements to 150 GPa. *J. physics: Conf. Ser.* **121** (2008).
4. Sun, T., Brodholt, J., Li, Y. & Vocadlo, L. Melting properties from *ab initio* free energy calculations: iron at the earth's inner-core boundary. *Phys. Rev. B* **98**, 224301 (2018).
5. Aquilanti, G. *et al.* Melting of iron determined by X-ray absorption spectroscopy to 100 GPa. *Proc. Natl. Acad. Sci.* **112**, 12042–12045 (2015).
6. Jackson, J. M. *et al.* Melting of compressed iron by monitoring atomic dynamics. *Earth Planet. Sci. Lett.* **362**, 143–150, DOI: [10.1016/j.epsl.2012.11.048](https://doi.org/10.1016/j.epsl.2012.11.048) (2013).
7. Morard, G. *et al.* Solving controversies on the iron phase diagram under high pressure. *Geophys. Res. Lett.* **45**, 11, 074 – 11, 082 (2018).
8. Sinmyo, R., Hirose, K. & Ohishi, Y. Melting curve of iron to 290 gpa determined in a resistance-heated diamond-anvil cell. *Earth Planet. Sci. Lett.* **510**, 45 (2019).
9. Hou, M. *et al.* Melting of iron explored by electrical resistance jump up to 135 gpa. *Geophys. Res. Lett.* **48**, e2021GL095739 (2021).
10. Li, J. *et al.* Shock melting curve of iron: A consensus on the temperature at the earth's inner core boundary. *Geophys. Res. Lett.* **47**, e2020GL087758 (2020).
11. Errandonea, D., Somayazulu, M., Hausermann, D. & Mao, H. Melting of tantalum at high pressure determined by angle dispersive x-ray diffraction in a double-sided laser-heated diamond-anvil cell. *J. Phys.: Condens. Matter* **15**, 7635–7649 (2003).
12. Dewaele, A., Mezouar, M., Guignot, N. & Loubeyre, P. High melting points of tantalum in a laser-heated diamond anvil cell. *Phys. Rev. Lett.* **104**, 29–31 (2010).
13. Burakovsky, L. *et al.* high pressure-high temperature polymorphism in ta: Resolving an ongoing experimental controversy. *Phys. Rev. Lett.* **104**, 255702 (2010).
14. Santamaria-Perez, D. *et al.* X-ray measurements of mo melting to 119 gpa and the high pressure phase diagram. *The J. Chem. Phys.* **130**, 124509 (2009).
15. Hrubciak, R., Meng, Y. & Shen, G. Microstructures define melting of molybdenum at high pressure. *Nat. Commun.* **8**, 14562 (2017).

16. Cazorla, C., Gillan, M., Taioli, S. & Alfé, D. Ab initio melting curve of molybdenum by the phase coexistence method. *The J. Chem. Phys.* **126**, 194502 (2007).
17. Anzellini, S. *et al.* In situ characterization of the high pressure- high temperature meltig curve of platinum. *Sci. Reports* **9**, 13034 (2019).
18. Errandonea, D. High-pressure melting curves of the transition metals Cu, Ni, Pd, and Pt. *Phys. Rev. B - Condens. Matter Mater. Phys.* **87**, 1–5, DOI: [10.1103/PhysRevB.87.054108](https://doi.org/10.1103/PhysRevB.87.054108) (2013).
19. Burakovsky, L., Chen, S., Preston, D. & Sheppard, D. Z methodology for phase diagram studies: platinum and tantalum as examples. *J. Phys.: Conf. Ser.* **500**, 162001 (2014).
20. Anzellini, S., Burakovsky, L., Turnbull, R., Bandiello, E. & Errandonea, D. P-v-t equation of state of iridium up to 80 gpa and 3100 k. *Crystals* **11**, 452 (2021).
21. Errandonea, D. *et al.* Experimental and theoretical confirmation of an orthorhombic phase transition in niobium at high pressure and temperature. *Commun. Mater.* **1**, 60 (2020).
22. Errandonea, D. *et al.* Melting curve and phase diagram of vanadium under high-pressure and high-temperature conditions. *Phys. Rev. B* **100**, 094111 (2019).
23. Steinitz, M., Schwartz, L., Marcus, J., Fawcett, E. & Reed, W. A. Lattice anysotropy in antiferromagnetic chromium. *Phys. Rev. Lett.* **23**, 979 (1969).
24. Umebayashi, H., Shirane, G., Frazer, B. & Daniels, W. Neutron diffraction study of cr under high pressure. *J. Phys. Soc. Jpn.* **24**, 368 (1968).
25. Mitsui, T. & Tomizuka, C. Effect of hydrostatic pressure on the neel temperature in chromium. *Phys. Rev.* **137**, A564 (1965).
26. Asano, S. & Yamashita, J. Ferromagnetism and Antiferromagnetism in 3d Transition Metals. *Progr. Theor. Phys.* **49**, 373 (1973).
27. Baty, S., Burakovsky, L. & Preston, D. Topological equivalence of the phase diagrams of molybdenum and tungsten. *Crystals* **10**, 20 (2020).
28. Söderling, P., Ahuja, R., Johansson, B. & Wills, J. Theoretical pprediction of structural phase transitions in Cr, Mo, and W. *Phys. Rev. B* (1994).
29. Ming, L. & Manghnani, H. Isothermal compression of bcc transition metlas to 100 kbar. *J. Appl. Phys.* **49**, 208 (1978).
30. Evenson, W. & Hall, H. Volume measurments on chromium to pressure of 30 kilobars. *Science* **150**, 1164 (1965).
31. Tkacz, M. high pressure studies of the fcc chromium hydride. *Rev. High Press. Sci. Technol.* **7**, 263–265 (1998).
32. Marizy, A., Geneste, G., Loubeyre, P., Guigue, B. & Garbarino, G. Synthesis of bulk chromium hydrides under pressure of up to 120 gpa. *Phys. Rev. B* **97**, 184103 (2018).
33. McQueen, R., Marsh, S., Taylor, J., Fritz, J. & Carter, W. *High-Velocity Impact Phenomena*, chap. VII - The equation of state of solids from shock wave studies (Academic Press, New York and London, 1970).
34. Young, D. *Phase diagram of the elements* (University of California Press, 1991).
35. Errandonea, D. *et al.* Systematics of transition-metal melting. *Phys. Rev. B* **63**, 132104 (2001).
36. Lord, O. *et al.* The melting curve of Ni to 1 Mbar. *Earth Planet. Sci. Lett.* **408**, 226–236 (2014).
37. Dewaele, A., Mezouar, M., Guignot, N. & Loubeyre, P. Melting of lead under high pressure studied using second-scale time-resolved x-ray diffraction. *Phys. Rev. B - Condens. Matter Mater. Phys.* **76**, 1–5, DOI: [10.1103/PhysRevB.76.144106](https://doi.org/10.1103/PhysRevB.76.144106) (2007).
38. Parisiades, P. A Review of the Melting Curves of Transition Metals at High Pressures Using Static Compression Techniques. *Crystals* **11**, 416 (2021).
39. Anzellini, S. *et al.* Phase diagram of calcium at high pressure and high temperature. *Phys. Rev. Mater.* **2**, 083608 (2018).
40. Xiong, L., Li, Q., Yang, C., Xie, Q. & Zhang, J. A high pressure study of cr₃c₂ by xrd and dft. *Chin. Phys. B* **29**, 086401 (2020).
41. Mougin, J., Bihan, T. L. & Lucazeau, G. high-pressure study of cr₂o₃ obtained by high-temperature oxidation by x-ray diffraction and raman spectroscopy. *J. Phys. Chem. Solids* **62**, 553 (2001).

42. Anzellini, S. & Boccato, S. A practical review of the laser-heated diamond anvil cell for university laboratories and synchrotron applications. *Crystals* **10**, 459 (2020).
43. Briggs, R. *et al.* High-pressure melting behavior of tin up to 105 gpa. *Phys. Rev. B* **95**, 054102 (2017).
44. Lord, O. T. *et al.* The NiSi melting curve to 70GPa. *Phys. Earth Planet. Interiors* **233**, 13–23, DOI: [10.1016/j.pepi.2014.05.005](https://doi.org/10.1016/j.pepi.2014.05.005) (2014).
45. Boccato, S. *et al.* The Melting Curve of Nickel Up to 100 GPa Explored by XAS. *J. Geophys. Res. Solid Earth* **122**, 1–10 (2017).
46. Burakovsky, L., Burakovsky, N. & Preston, D. Ab initio melting curve of osmium. *Phys. Rev. B* **92**, 174105 (2015).
47. Stankus, S. Density of vanadium and chromium at high temperature. *high temp.* **31**, 684 (1993).
48. Abrikosov, I., Ponomareva, A., Steneteg, P., Barannikova, S. & B. Alling. Recent progress in simulations of the paramagnetic state of magnetic materials. *Curr. Opin. Solid State Mater. Sci.* **20**, 85–106 (2016).
49. Gorecki, T. Vacancies and a generalised melting curve of metals. *high temperature - high pressure* **11**, 683 (1979).
50. Gurvich, L., Veits, I. & Medvedev, V. *Calculations of thermodynamic properties* (Nauka, Moscow, 1982).
51. Anzellini, S., Alfé, D., Pozzo, M. & Errandonea, D. Melting line of calcium characterized by in situ LH-DAC XRD and first-principle calculations. *Sci. Reports* **11**, 15025 (2021).
52. Alfé, D., Vocadlo, L., Price, G. D. & M J Gillan. Melting curve of materials : theory versus experiments. *J. Physics: Condens. Matter* **16**, S973–S982 (2004).
53. Japel, S., Schwager, B., Boehler, R. & Ross, M. Melting of copper and nickel at high pressure: The role of d electrons. *Phys. Rev. Lett.* **95**, 1–4 (2005).
54. Anzellini, S., Dewaele, A., Occelli, F., Loubeyre, P. & Mezouar, M. Equation of state of rhenium and application for ultra high pressure calibration. *J. Appl. Phys.* **115**, 043511, DOI: [10.1063/1.4863300](https://doi.org/10.1063/1.4863300) (2014).
55. Jenei, Z. *et al.* Single crystal toroidal diamond anvils for high pressure experiments beyond 5 megabar. *Nat. Commun.* **9** (2018).
56. Loubeyre, P. *et al.* Equation of state and phase diagram of solid ⁴He from single-crystal x-ray diffraction over large p-t domain. *Phys. Rev. Lett.* **71**, 2272 (1993).
57. White, G., Smith, T. & Carr, R. Thermal expansion of Cr, Mo and W at low temperature. *Cryogenics* **18**, 301–303 (1978).
58. Guo, G. & Wang, H. Calculated elastic constant and electronic and magnetic properties of bcc, fcc and hcp Cr crystals and thin films. *Phys. Rev. B* **62**, 5136 (2000).
59. Skriver, H. The electronic structure of antiferromagnetic chromium. *J. Phys. F: Met. Phys.* **11**, 97 (1981).
60. Jaramillo, R. *et al.* Breakdown of the Bardeen-Cooper-Schrieffer ground state at a quantum phase transition. *Nature* **459**, 405 (2009).
61. Dorogokupets, P. I. & Oganov, A. R. Ruby, metals, and MgO as alternative pressure scales: A semiempirical description of shock-wave, ultrasonic, x-ray, and thermochemical data at high temperatures and pressures. *Phys. Rev. B* **75**, 024115, DOI: [10.1103/PhysRevB.75.024115](https://doi.org/10.1103/PhysRevB.75.024115) (2007).
62. Abrikosov, I., Ponomareva, A., Steneteg, P., Barannikova, S. & Alling, B. Recent progress in simulations of the paramagnetic state of magnetic materials. *Curr. Opin. Solid State Mater. Sci.* **20**, 85–106 (2016).
63. Dudarev, S., Botton, G., Savrasov, S., Humphreys, C. & Sutton, A. Electron-energy-loss spectra and the structural stability of nickel oxide: An LSDA+U study. *Phys. Rev. B* **57**, 1505 (1998).
64. Aryasetiawan, F., Karlsson, K., Jepsen, O. & Schönberger, U. Calculations of Hubbard U from first-principle. *Phys. Rev. B* **74**, 125106 (2006).
65. Angel, R. J., Gonzalez-platas, J. & Alvaro, M. EosFit7c and a Fortran module (library) for equation of state calculations. *Z. Kristallogr.* **229**, 405–419 (2014).
66. Lee, S. & Horita, Z. *Mater. Transactions Sci.* **53**, 38–45 (2012).
67. Berman, R. Internally-consistent thermodynamic data for minerals in the system Na₂O-K₂O-CaO-MgO-FeO-Fe₂O₃-Al₂O₃-SiO₂-TiO₂-H₂O-CO₂. *J. Petrol.* **29**, 445–522 (1988).
68. Anzellini, S. *et al.* Thermal equation of state of ruthenium characterized by resistively heated diamond anvil cell. *Sci. Reports* **10**, 7092 (2020).

69. Swenson, C. Equation of state of cubic solids; some generalizations. *J. Phys. Chem. Solids* **29**, 1337–1348 (1968).
70. Dewaele, A., Loubeyre, P. & Mezouar, M. Equations of state of six metals above 94 GPa. *Phys. Rev. B* **094112**, 1–8 (2004).
71. Holzapfel, W. Refinement of the ruby luminescence pressure scale. *J. Appl. Phys.* **93**, 1813 (2003).
72. Anzellini, S. *et al.* Laser-heating system for high-pressure x-ray diffraction at the extreme condition beamline i15 at diamond light source. *J. Synchrotron Radiat.* **25** (2018).
73. Dewaele, A. *et al.* High-pressure-high-temperature equation of state of KCl and KBr. *Phys. Rev. B - Condens. Matter Mater. Phys.* **85**, 1–7, DOI: [10.1103/PhysRevB.85.214105](https://doi.org/10.1103/PhysRevB.85.214105) (2012).
74. Benedetti, L. & Loubeyre, P. Temperature gradients, wavelength-dependent emissivity, and accuracy of high and very-high temperatures measured in the laser-heated diamond cell. *High Press. Res.* **24**, 423–445 (2004).
75. Prescher, C. & Prakapenka, V. Dioptas: a program for reduction of two-dimensional x-ray diffraction data and data exploration. *High Press. Res.* **35**, 223 (2015).
76. Coelho, A. Topas and topas-academic: an optimization program integrating computer algebra and crystallographic object written in c++. *J. Appl. Crystallogr.* **51**, 210 (2018).
77. Blöchl, P. E. Generalized separable potentials for electronic-structure calculations. *Phys. Rev. B* **41**, 5414–5416 (1990).
78. Perdew, J. P., Burke, K. & Ernzerhof, M. Generalized gradient approximation made simple. *Phys. Rev. Lett.* **77**, 3865–3868 (1996).
79. Chen, J., Singh, D. & Krakauer, H. Local-density description of antiferromagnetic Cr. *Phys. Rev. B* **38**, 12834 (1988).
80. Fawcett, E. Spin-density-wave antiferromagnetism in chromium. *Rev. Mod. Phys.* **60**, 209 (1988).
81. Wang, C., Klein, B. & Krakauer, H. Theory of Magnetic and Structural Ordering in Iron. *Phys. Rev. Lett.* **54**, 1852 (1985).
82. Guo, G., Ebert, H., Temmerman, W., Schwarz, K. & Blaha, P. Relativistic effects on the structural and magnetic properties of iron. *Solid State Commun.* **79**, 121–124 (1991).
83. Bagno, P., Jepsend, O. & Gunnarsson, O. Ground state properties of third-row elements with nonlocal density functionals. *Phys. Rev. B* **40**, 1997(R) (1989).
84. Barbiellini, B., Moroni, E. & Jarlborg, T. Effects of gradient corrections on electronic structure metals. *J. Phys. Condens. Matter* **2**, 7597 (1990).
85. Moroni, E., Kresse, G., Hafner, J. & Furthmüller, J. Ultrasoft pseudopotentials applied to magnetic Fe, Co, and Ni: From atoms to solids. *Phys. Rev. B* **56**, 15629 (1997).
86. Hobbs, D., Kresse, G. & Hafner, J. Fully unconstrained noncollinear magnetism within the projector augmented-wave method. *Phys. Rev. B* **62**, 11556 (2000).
87. Burakovsky, L., Lusher, D., Preston, D., Sjue, S. & Vaughan, D. Generalization of the Unified Analytic Melt-Shear Model to Multi-Phase Materials: Molybdenum as an Example. *Crystals* **9**, 86 (2019).
88. Belonoshko, A. B. *et al.* Xenon melting : Density functional theory versus diamond anvil cell experiments. *Phys. Rev. B* **74**, 054114 (2006).

Acknowledgements

The authors acknowledge the DLS synchrotron facility for provision of beamtime on the beamlines I15 (exp. CM26452-2 and CY28469-1). D.E. is thankful for the financial support to this research from the Spanish Ministerio de Ciencia, Innovación y Universidades, the Spanish Research Agency, and the European Fund for Regional Development under PID2019-106383GB-C41 and RED2018-102612-T (MALTA Consolider-Team Network) and by Generalitat Valenciana through the grant Prometeo/2018/123 EFIMAT.

Author Contributions

S.A. and D.E. conceived the experiment. S.A. conducted the HP-HT experiment. S.A. and J.E.P. conducted the cold compression experiment. S.A. and D.E. analyzed the results. L.B. performed the theoretical calculations. The manuscript is written through contributions of all authors. All authors have given approval to the final version of the manuscript.

Additional Information

Competing Interests: The authors declare no competing interests.